Progress in aerodynamic and aeroacoustic integration of CROR propulsion systems

A. Stuermer
arne.stuermer@dlr.de
J. Yin and R. Akkermans
DLR Institute of Aerodynamics and Flow Technology
Lilienthalplatz, Braunschweig
Germany

ABSTRACT

Contra-Rotating Open Rotor (CROR) propulsion systems have seen renewed interest as an economic and environmentally friendly powerplant for future transport aircraft. Installation effects, i.e. the mutual interactions between airframe components and the rotors, have a pronounced impact on the aerodynamic and aeroacoustic performance for this type of engine. In the past five years, DLR's Institute of Aerodynamics and Flow Technology has performed a number of numerical studies investigating important aspects relating to engine-airframe integration of CROR engines. In this article an overview of coupled aerodynamic and aeroacoustic simulations investigating representative pusher-configuration CROR engines will be given, focusing on the impact on aerodynamic performance and aeroacoustics caused by the presence of a pylon, the potential for noise reduction by employing trailing-edge blowing at the pylon trailing edge as well as the performance and noise variations caused by different senses of rotation of the rotors. It is shown that the interaction with the pylon strongly impacts blade performance and front rotor noise emissions but that the use of active flow control in the form of pylon trailing-edge blowing can alleviate these adverse installation effects to a notable extent.

Paper No. 4078. Manuscript received 13 August 2013, revised version received 20 November 2013, accepted 21 November 2013.
This paper is based on a presentation made at the *Progress Towards Open Rotor Propulsion Technology* Conference held at the RAeS HQ in London, 21 November 2012.

https://doi.org/10.1017/S0001924000009829 Published online by Cambridge University Press

NOMENCLATURE

B_A, B_F	aft, front rotor blade passing frequency
c	chord length
$C_{F,1P}$	in-plane rotor force coefficient, $C_{F,1P} = (C_Y^2 + C_Z^2)^{0.5}$
C_F	total blade loading coefficient, $C_{F,1P} = (C_x^2 + C_Y^2 + C_Z^2)^{0.5}$
C_L	lift coefficient, $C_L = F_z/(qS)$
C_P	power coefficient, $C_P = P/(\rho n^3 D^5)$
$C_{T,Y,Z}$	thrust, lateral and lift coefficient, $C_{T,Y,Z} = F_{x,y,z}/(\rho n^2 D^4)$
D	front rotor diameter
f	frequency
$F_{x,y,z}$	forces in Cartesian co-ordinate system
M	Mach number
n	rotor rotational frequency
P	power
q	dynamic pressure, $q = 0{\cdot}5\rho V_0^2$
r	radial position
R	rotor radius
S	reference area
t	aerofoil thickness
V_0	freestream velocity
x,y,z	Cartesian co-ordinate system positions

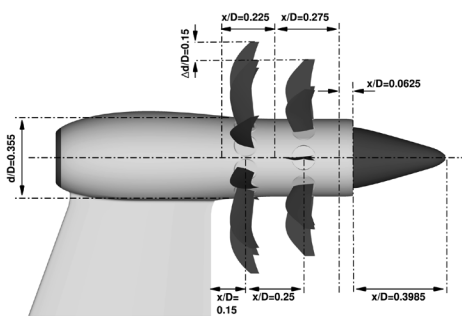
Greek Symbols

α	angle-of-attack
β_{75}	blade pitch angle at 75% radius
η	rotor efficiency
Ψ	Azimuth angle
ρ	density
θ	polar angle
ω	angular velocit

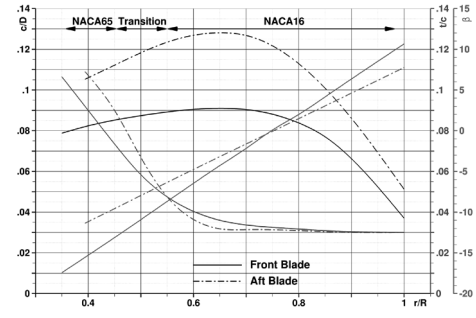
Abbreviations

1P	Once per rotor revolution
BPF	Blade Passing Frequency
CROR	Contra-Rotating Open Rotor
DBP	Down Behind Pylon
EPNL	Effective Perceived Noise Level
FW-H	Ffowcs Williams-Hawkings
SPL	Sound Pressure Level
UBP	Up Behind Pylon
uRANS	Unsteady Reynolds Averaged Navier-Stokes

https://doi.org/10.1017/S0001924000009829 Published online by Cambridge University Press



(a) Geometric layout of the propulsion system



(b) Blade design characteristics

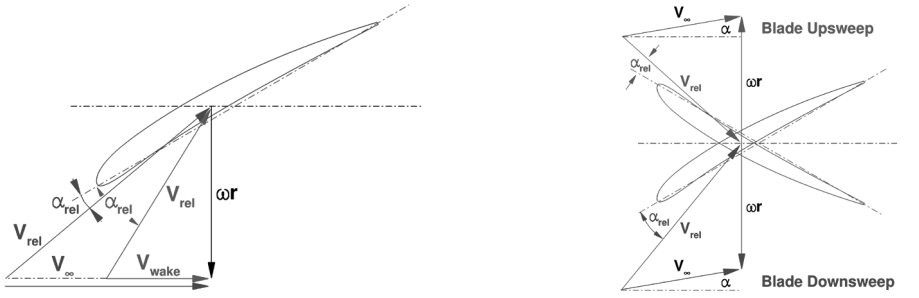
Figure 1. Generic pusher CROR configuration geometry and design characteristics.

1.0 INTRODUCTION

Increasing environmental and economic pressures have renewed interest in Contra-Rotating Open Rotor (CROR) propulsion systems as a powerplant for future commercial transport aircraft, as they promise a step change in efficiency versus modern turbofan engines. These powerplants had been the focus of a large research program led by NASA and US industry in the late 1970s and 1980s[1]. As oil costs reduced to levels similar to those prior to the 1973 oil crisis, interest in bringing these engines to market waned. With fuel again becoming an increasingly dominant part of an airline's operating costs and a growing focus on aviation's environmental impact, current research efforts aiming at the realisation of a commercially viable Open Rotor engine are focusing on the issues of noise emissions and installation effects with the airframe. The former is an important issue during the low-speed take-off and approach phases of flight, where acceptable community noise levels need to be ensured. The rapid improvement of modern numerical aerodynamic and aeroacoustic simulation tools such as the DLR TAU and APSIM-Codes allow these methods to play a vital role in enhancing understanding and developing solutions for these issues[2,3].

In a series of numerical studies, a representative CROR powerplant in pusher configuration was investigated as a numerical test rig to allow for the study of relevant parameters that affect the aerodynamic and aeroacoustic performance. The engine design was aimed at a take-off thrust requirement of F_x = 88kN at sea level conditions and cruise thrust of F_x = 19kN for M = 0·75 flight at 35,000ft, making it representative of a powerplant for typical single-aisle aircraft in the 150-seat class. The general layout of the powerplant is shown in Fig. 1(a) and includes the core engine air intake and exhaust, for which an engine boundary condition can be applied in the DLR TAU-Code to produce realistic jet and inlet flowfields. Having studied a number of different rotor configurations[4,5], the present investigation is focused on a 10 × 8-bladed design, with a front rotor diameter of D = 4·2672m and an aft rotor with a diameter reduction of 15% with a rotor-to-rotor spacing of x/D = 0·25. Figure 1(b) plots the characteristic design parameters chord (c/D), thickness (t/c) and twist distribution (β) of the front and aft blades, which feature NACA65-series aerofoils from the root to the radial position of r/R = 0·45 and then transition to NACA16-series aerofoils, which are used from r/R = 0·55 outward. Figure 1(a) shows the powerplant with a representative pylon intended for the installation on the aft fuselage of an aircraft. The pylon aerofoil, with a relative thickness of t/c = 0·1, is a symmetric design found in literature[6]. The installation was designed

https://doi.org/10.1017/S0001924000009829 Published online by Cambridge University Press



(a) Pylon wake impact on blade flow properties (b) Angle-of-attack impact on blade flow

Figure 2. Installation effects on rotor and blade flow for pusher CROR installations.

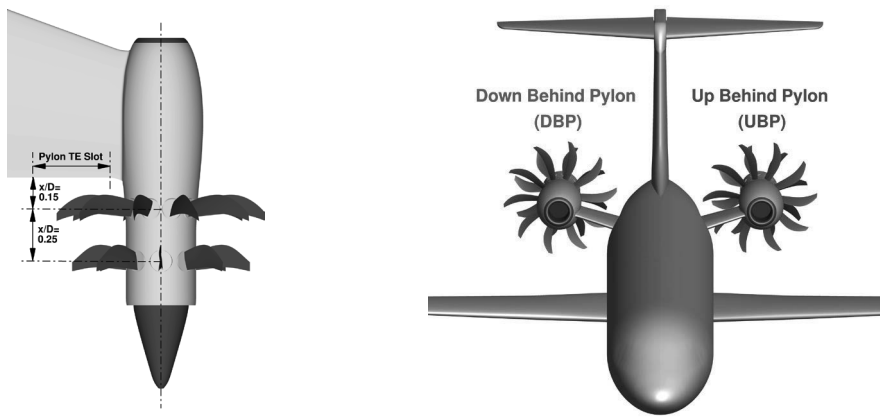
to avoid strong shocks as well as flow separation at the trailing edge in the nacelle-pylon junction at the cruise design point, impacting the pylon planform as well as the pylon-nacelle integration. The adopted pylon planform features a leading edge sweep of 15° with no twist and is attached to the nacelle with a spacing of $x/D = 0{\cdot}15$ between the pylon trailing edge and the front rotors plane of rotation. The choice of a pusher configuration for this type of propulsion system is driven by considerations regarding both cabin noise and certification issues relating to blade loss scenarios as well as the avoidance of potentially large installation drag increases, which can be expected due to the interaction of the propeller slipstream with the wing for more conventional wing-mounted tractor configurations[7]. Naturally some potentially negative trade-offs are also incurred, which are one of the primary focus areas investigated in the present research. One such aspect is the possibility of increased trim drag, in part due to the in-plane forces generated by the propellers at non-uniform inflow conditions, which may have a more substantial moment arm with respect to the aircraft centre of gravity for an empennage installation. One inherent disadvantage of the pusher-type installation is the interaction of the pylon wake with the rotors. As sketched in Fig. 2(a), the pylon wake is characterised by a velocity deficit versus the mean flow, which leads to an abrupt and localised increase in blade effective incidence angle during the latter's passage aft of pylon trailing edge. This incurs an unsteady loading component for the blade, which in turn results in increased noise emissions in comparison with an uninstalled or tractor-configuration CROR engine. Also, while the global inflow to the rotors of a pusher-type installation will generally be subject to less distortion in terms of incidence angle due to the avoidance of a direct interaction with the wing upwash that occurs for a wing-mounted tractor configuration, the inflow will still show substantial non-uniformity in both incidence and sideslip angle due to the complex flowfield around the aircraft empennage. As sketched in Fig. 2(b) for the example of a rotor at some non-zero angle-of-attack, such effects lead to an asymmetric loading of the blades during their rotation. For the sketched case, a blade on its downward sweep will be subjected to an increased effective incidence angle, while a diametrically opposed blade sees a lower incidence angle. This again leads to an unsteady load for the blade and thus also to additional noise emissions.

These two installation associated effects are of primary concern for pusher-CROR aircraft configurations. The alleviation or elimination of the extraneous noise (as well as concerns regarding blade structural fatigue due to unsteady loading) caused by the impingement of the pylon wake on the rotors was the focus of a study investigating pylon trailing-edge blowing. The application of active blowing to reduce unsteady aerodynamic loadings and the associated increases in tonal noise has been shown to be a viable technology in related turbomachinery applications[8] and recently also experimentally for CROR applications[9]. The challenge of

https://doi.org/10.1017/S0001924000009829 Published online by Cambridge University Press

trailing-edge blowing application to the pylon of a pusher configuration CROR propulsion system lies in the close coupling of the pylon with the rotors, as can be seen in Fig. 3(a). Thus the mixing length, during which the injected air can serve to fill the pylon wake deficit is limited, and the full alleviation of the adverse impact of the wake on the rotor is non-trivial. In this study, a slot in the trailing edge is introduced between the span positions of $0{\cdot}5 < y/R < 1{\cdot}2$ (see Fig. 3(a), through which air is blown with the aim of filling the wake deficit. Principal results of this investigation are discussed in Section 3. Another important issue for installed pusher CROR engines is shown in Fig. 3(b), where an expected typical installation of the CRORs on the empennage of a notional future single-aisle category aircraft, in this case the DLR LamAiR aircraft configuration[10], is plotted. As is common for commercial turboprop aircraft, the sense of rotation of the CROR rotors on either side of the aircraft is most likely to be identical, i.e. with an up-behind-pylon (UBP) sense of rotation of the front rotor on the one and a down-behind-pylon (DBP) sense of rotation on the other side of the aircraft. A common reason for such a design choice is the elimination of the need to design, build and have available duplicate engine components (gearbox parts, blades) to enable counter rotation of the engine rotors on the left and right side of the fuselage. This results in a geometrically asymmetric aircraft and, due to the strong interactions between the open rotors and the airframe, also in some notable peculiarities in the aircraft aerodynamics, handling qualities and the noise emissions. The main outcomes of an investigation into these issues[11] are elucidated in Section 4.

Both studies, which to the authors' knowledge are the first investigations of these installation effects in general for the latter or by numerical means for the former case, will show the benefit that can be drawn from the depth of information yielded by high-fidelity numerical simulations. The potential of active flow control to alleviate the adverse impact in terms of additional unsteady blade loading and increased front rotor noise emissions due to the pylon-rotor interaction for pusher CROR configurations will be highlighted. Additionally, a clearly preferable sense of rotation direction for the installation of pusher-CROR engines on an aircraft empennage is identified and the consequences on rotor performance, aircraft handling qualities and noise emissions of choosing an asymmetric installation of this type of engine are discussed.



(a) Geometric setup for the pylon trailing edge blowing study

(b) Example of a typical CROR propulsion system integration on the empennage of an aircraft resulting in asymmetric rotor rotation

Figure 3. CROR configurations for the analysis of characteristic installation effects.

https://doi.org/10.1017/S0001924000009829 Published online by Cambridge University Press

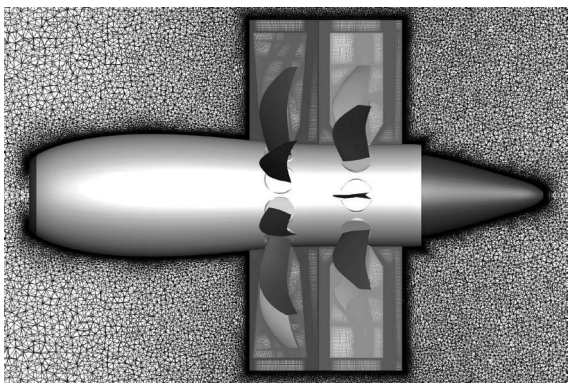
2.0 NUMERICAL APPROACH

For all studies discussed here a coupled simulation utilising the DLR TAU-Code for the unsteady CFD computations and the DLR APSIM-Code for a subsequent prediction of the noise emissions is performed.

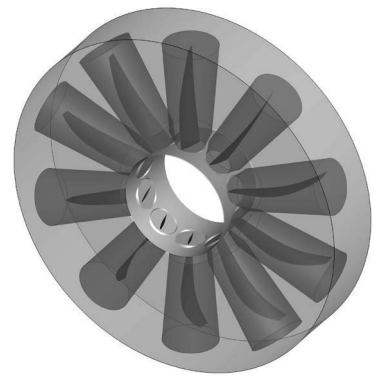
2.1 DLR TAU unsteady CFD simulation approach

The DLR TAU-Code is an unstructured finite-volume vertex-based CFD solver. For the CROR simulations spatial discretisation of the convective fluxes is done using a second order central differencing scheme with scalar dissipation while the viscous fluxes are discretised with central differences. Turbulence is modeled with the 1-equation model of Spalart-Allmaras[12]. The dual time approach is used to compute unsteady flows[13] and the relative motion of the rotors is specified through the use of the codes Chimera capability as well as the implemented motion libraries[14].

For all of the generic semi-installed pusher CROR simulations the flexibility afforded by the Chimera approach was fully exploited and an approach of using this method to enable arbitrary blade pitch settings was devised. The meshes consist of a total of 21 Chimera blocks, with an overview of the mesh shown in Fig. 4(a). The first mesh block is for the nacelle-pylon part of the propulsion system, which was generated using the CentaurSoft Centaur mesh generation software. The mesh generation exploits the symmetry of the configuration, and a hybrid unstructured mesh is created for half of the pylon-nacelle configuration, which ensures spatial discretisation in the CFD simulation is also symmetric along the horizontal plane. Hexahedral or prismatic layers are used on all surfaces of the nacelle, with appropriate settings for the initial cell and overall stack height to obtain an adequate resolution of the boundary layers in the simulations. Refined mesh regions are set in the rotor in – and outflow and the pylon wake region. The obtained Centaur mesh for the pylon-nacelle is then subsequently mirrored to obtain the final complete nacelle mesh. The rotor meshes are structured meshes, which were generated using the ANSYS ICEM CFD mesh generation software. The geometric setup of the rotor and blades enabling flexible setting of the blade pitch is shown for the example of the 10-bladed front rotor in Fig. 4(b). The gray translucent surface represents the Chimera boundary of the rotor, while the blue translucent frustums are the Chimera boundaries of the individual blades. The periodic nature of the geometry was exploited, and a mesh was generated for a 45° or 36°-slice of the aft and front rotors respectively and



(a) Chimera blocking strategy and overall mesh setup



(b) Rotor Chimera blocking strategy

Figure 4. Modular Chimera meshing approach for the semi-installed CROR configuration.

https://doi.org/10.1017/S0001924000009829 Published online by Cambridge University Press

subsequently completed to the full annulus. The blade meshes are structured hexahedral meshes, again generated using ICEM CFD. A c-grid topology is used to wrap around the blade and fit into the frustum Chimera boundary. For each rotor, a single blade mesh is created and the blading for each rotor results through the appropriate rotation and translation of this grid. Identical mesh settings were used for both the front and aft rotors blades. The complete multi-block Chimera mesh of the semi-installed CROR, that was used both in the pylon trailing-edge blowing and the sense of rotation investigations, consist of just fewer than 48 million nodes.

The uRANS computations at each angle-of-attack are initialised with a steady-state simulation in which the blades are pitched to a low-drag setting. The pitches in the unsteady runs are then set to an initial angle based on knowledge of the individual blade performance. In the course of the simulation the time step size is incrementally reduced to a final value equivalent to a propeller rotation of $\Delta\Psi = 0{\cdot}5°$ per physical time step. During the simulations, the total thrust production as well as the loading balance between the two rotors is periodically evaluated and the blade pitch setting adapted to obtain the desired operating point for each case. Convergence in terms of periodicity in both the rotor as well as the pylon forces was achieved after 14 full rotor rotations. Total runtime for each of the computations using 384 nodes of DLRs 6000-core C2A2S2E-cluster in Braunschweig was around 21 days.

2.2 DLR APSIM-code aeroacoustic simulations

The Aeroacoustic Prediction System based on Integral Method (APSIM) was developed at the DLR Institute of Aerodynamics and Flow Technology for the prediction of rotor and propeller noise radiated in the free farfield[3,15,16]. APSIM is based on the Ffowcs Williams-Hawkings (FW-H) permeable or impermeable surface as well as the Kirchhoff formulations[17,18]. The code is designed to calculate wave propagation over large distances in uniform flows and therefore does not account for non-linear propagation effects outside of the integral surface. The time-domain APSIM-calculations draw on unsteady CFD input data and deliver a pressure time history at any desired observer location, which can be Fourier analysed to derive acoustic spectrum data.

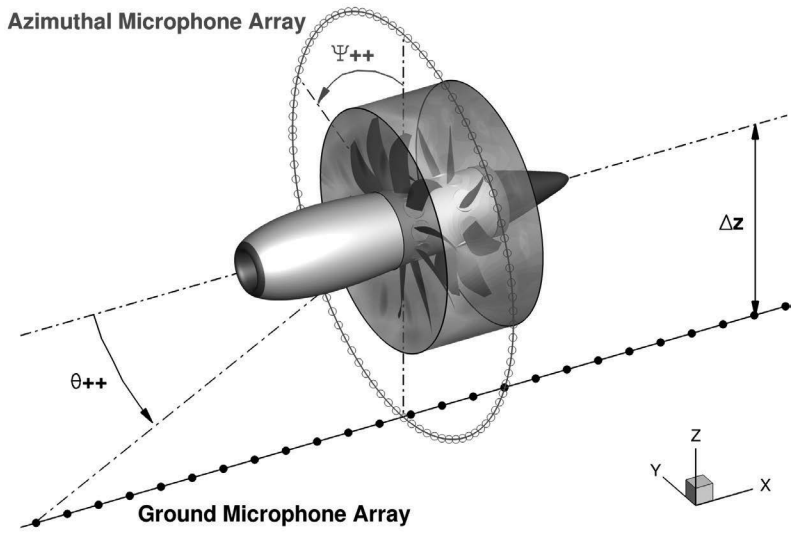


Figure 5. APSIM aeroacoustic analysis setup.

https://doi.org/10.1017/S0001924000009829 Published online by Cambridge University Press

The FW-H permeable surface approach applied in the present investigations uses uRANS CFD input data on virtual, arbitrary surfaces, which enclose the relevant noise sources. In general, the large size of these virtual surfaces makes this approach preferable as it can include volumetric sources (quadruple). However, the location of the permeable surface must be carefully chosen with respect to the resolution of the CFD grid, to ensure that the mesh element sizes are sufficiently small to allow for the propagation of the acoustic waves in the frequency range of interest from the noise source to the integral surface. In the current applications, the nacelle Chimera boundary, shown as the translucent surface in Fig. 5, is used as the permeable input surface to APSIM. This choice was made out of practical considerations, since this boundary represents an already existing closed surface which fully encloses the rotors as the dominant noise source. The noise contribution of the nacelle and pylon, which lie outside of this permeable surface, are not considered in the present APSIM computations.

The major open rotor noise components are thickness (monopole) noise (due to the volume displacement of the blades), steady-loading noise (due to the steady forces on the blades), unsteady-loading noise (due to circumferentially non-uniform loading), quadruple (nonlinear) noise, and broadband noise. CRORs feature all sources of noise known for the single rotation propeller, but the aerodynamic interactions between the two rotors as well as the installation impact gives rise to additional significant levels of unsteady loading noise, leading to the so-called interaction tones. The frequency components of the interaction tones are related to the blade passing frequencies (BPF) of both the front and rear rotor. Although broadband noise can be important for some flight conditions, it is believed to be less important than the tonal noise components and is not considered in the present simulations.

In this article the aeroacoustic results are evaluated for a ground microphone array line at a distance of ten front rotor diameters from the engine axis, shown as the black line in Fig. 5, which is centred on the centre of the front rotor. The microphones located on this farfield microphone line are of particular interest as they relate to the flyover certification point.

3.0 PYLON BLOWING

For the study on pylon wake alleviation through the application of trailing-edge blowing, the semi-installed CROR configuration was investigated at typical M = 0·2 take-off flight conditions – an operating point where community noise plays an important role. The rotational speeds of both rotors are set identically to n = 1,100rpm, while the blade pitch settings to achieve the F_x = 88kN take-off thrust with the target power split of P_F/P_A = 1·25 are 34·85° and 41·40° for the front and aft rotors respectively.

3.1 Aerodynamic analysis

The motivation of applying pylon trailing-edge blowing as a means of active flow control for installed pusher CROR propulsion systems is evident in Fig. 6, which shows the development of the pylon wake at an axial position of x/D = 0·1 upstream of the front rotor in terms of the mean dynamic pressure profiles at radial positions of r/R = 0·5, 0·75 and 1·0 along the span of the pylon. The comparison shows that the isolated CRORs inflow is characterised by the acceleration of the air by the front rotor. The inclusion of the pylon leads to a strong localised flow velocity reduction due to the pylon wake. This perturbation of the rotor inflow causes a periodic increase in blade effective incidence angle as the blades pass through the pylon wake, with resulting pronounced unsteady loadings. The injection of air through the trailing edge along the pylon span serves to

https://doi.org/10.1017/S0001924000009829 Published online by Cambridge University Press

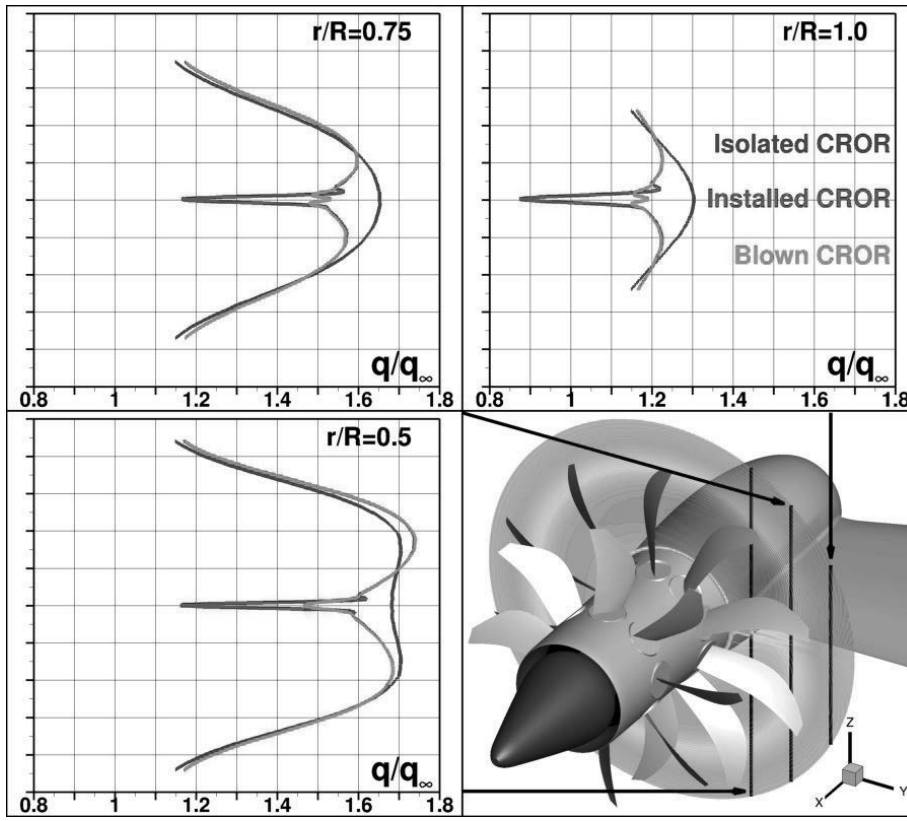
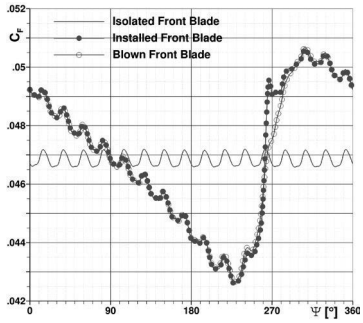


Figure 6. Dynamic pressure profiles at an upstream axial position of x/D = 0·1 relative to the front rotor rotational plane.

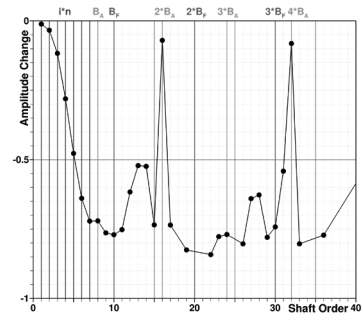
significantly reduce the wake deficit, while a recovery of the unperturbed isolated CRORs inflow has not been fully achieved. In this study the massflow of air through the pylon trailing edge is 2kg/s, a value that was found to result in good wake filling in a steady-state RANS analysis. The overall mean performance parameters of the CROR at the present operating point are practically unaffected by the application of the active flow control technique. Overall thrust drops from F_x = 88·191kN to F_x = 88·137, the power split shifts slightly from P_F/P_A = 1·2467 to P_F/P_A = 1·2471, while overall efficiency remains constant at η = 57·83%.

Figure 7(a) shows a comparison of the front rotor blade loading coefficient development during one full rotation. The isolated CRORs blade unsteady loadings are caused by the rotor-rotor interactions due to the aft blades potential flow field impact. The installation effect of the pylon leads to an overall 1P-loading cycle for the blades, dominated by an abrupt loading increase during passage through the wake. A similar effect is also found for the aft rotor blades, but at a significantly reduced magnitude. Thus the focus in this discussion is placed on the front rotor. The pylon trailing-edge air injection is seen to ameliorate the severity of this wake deficit driven loading increase, but as already implied by the wake profile comparison in Fig. 6, a 1P-loading cycle is still evident. Figure 7(b) shows the pylon blowing impact on the blade loading amplitude spectra, plotted as the relative change in fluctuation amplitude for the blown

https://doi.org/10.1017/S0001924000009829 Published online by Cambridge University Press



(a) Comparison of installation impact on the blade loading during one full front rotor revolution



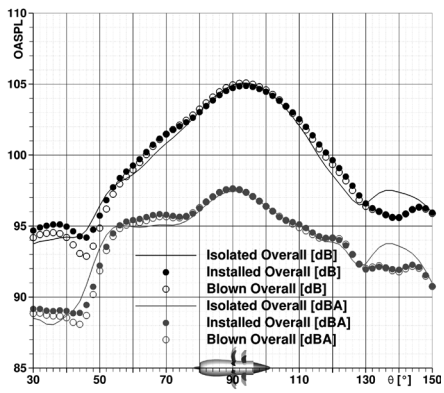
(b) Impact of pylon blowing on the installed CROR blade loading spectrum and fluctuation amplitude

Figure 7. Pylon and pylon blowing impact on reference front rotor blade loading development.

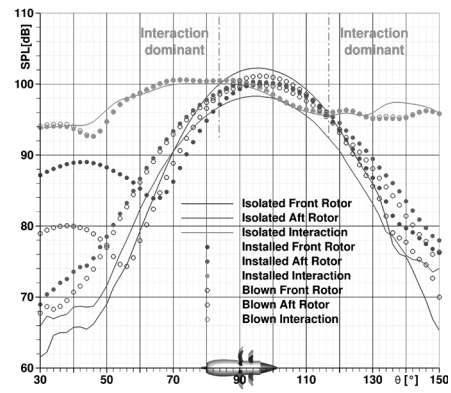
case versus the installed CROR without blowing. For the front rotor, the unsteady loadings are strongly reduced at higher harmonics of the shaft rotational speed, with the exception of frequencies corresponding to the even number higher-harmonics of the aft rotors blade passing frequency BA. This shows that – as can be expected – the rotor-rotor interactions, i.e. the upstream influence of the aft blades potential flow on the blades of the front rotor, are not significantly impacted by the pylon wake filling. As both the wake profiles and the blade loading development already indicated that a 1P-loading cycle still remains for the present blown pylon configuration, the reduction in blade loading oscillations at the shaft rotation speed n is not very significant in comparison with the installed CROR without pylon blowing.

3.2 Aeroacoustic analysis

The farfield noise emission directivities as computed in an APSIM analysis are plotted in Fig. 8. Figure 8(a) shows the CROR-characteristic relatively flat noise directivity in terms of the overall sound pressure levels with and without A-weighting. This typical directivity is driven in large part by interaction tones, which result due to the mutual influence the front and aft



(a) Comparison of overall and A-weighted ground noise emissions



(b) Decomposition of directivities into rotor associated and interaction tone components

Figure 8. Ground microphone analysis of installation and pylon blowing impact on CROR noise emissions.

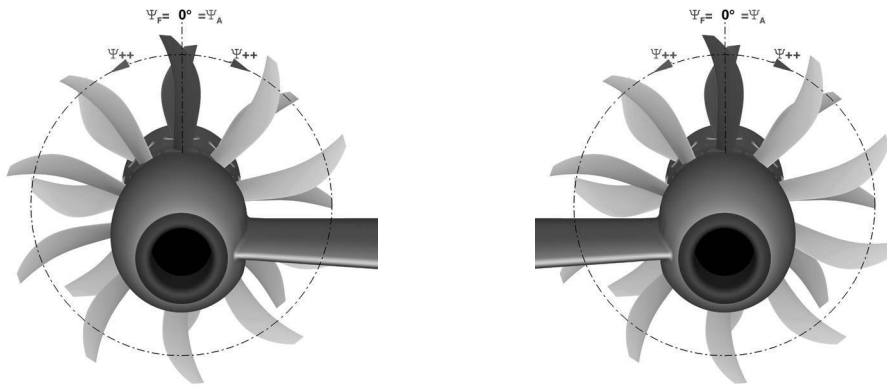
https://doi.org/10.1017/S0001924000009829 Published online by Cambridge University Press

rotor have on each other. With their root cause lying in this unsteady loading, they exhibit less focused noise directivities than the rotor tones. Therefore they play the dominant role in the up – and down-stream noise radiation. A small net benefit in terms of noise emissions is found for the installed case with pylon blowing versus the case without active flow control. Generally noise levels for the former case are quite comparable with the isolated case in the direct vicinity of the rotors and also in the upstream direction. A detailed analysis of the tone contributions to the ground noise emissions is shown in Fig. 8(b), which compares the front – and aft-rotor associated and the rotor-rotor interaction caused tone directivities for the three investigated configurations. The major impact of the pylon-wake-rotor interaction is an increase in the front rotor tones radiated in the upstream direction. The aft rotor associated tones and, in particular, the interaction tones are seen to be practically unaffected by this particular installation effect. This is in accordance with the blade force fluctuation spectra discussed for Fig. 7, where blade-blade interactions were found to show little difference between the isolated and installed configurations. The beneficial effect of the pylon wake alleviation through trailing-edge blowing is clearly seen in the reduction of front rotor associated tone levels by almost 10dB in the upstream arc versus the installed case without pylon blowing. This is already a significant benefit, even though the reductions fail to fully match the noise levels of the isolated CROR.

4.0 CROR SENSE OF ROTATION

As discussed in the previous section, the pylon has a very pronounced influence on a pusher CROR propulsion system. For an installation on the aircraft, in addition to this interaction with the pylon, angle-of-attack effects as well as non-uniform rotor inflow due to the complex aircraft flowfield (wing downwash, empennage and tail flow) are also of prime importance.

In this interaction, the sense of rotation of the (front) rotor with respect to the pylon plays an important role in both the aerodynamic and aeroacoustic performance of the propulsion system. Figure 9 shows the two possible scenarios of a pusher CROR installation along with the definition of the front and aft reference blade azimuthal position naming conventions. In Fig. 9(a), a down-behind-pylon (DBP) sense of rotation of the front rotor is shown, which means that a front rotor blade passes behind the pylon on its' downward sweep at an azimuthal angle of $\Psi = 90°$.



(a) Down behind pylon (DBP) front rotor rotation (b) Up behind pylon (UBP) front rotor rotation

Figure 9. Sense of rotation direction dependent definition of rotor and blade azimuthal angle.

https://doi.org/10.1017/S0001924000009829 Published online by Cambridge University Press

The effectively opposite sense of rotation, which would result for the installation of an identical engine on the other side of the aircraft empennage (see also Fig. 3(b)), results in an up-behind-pylon sense of rotation of the front rotor. Here front blade and pylon interact at an azimuthal position of $\Psi = 270°$. The simulations are performed at typical take-off conditions with a flight velocity of M = 0·20 at sea level. For reference all the relevant engine operating condition data in terms of angle-of-attack (α), front and aft rotor rotational speeds (n_F and n_A) and the respective blade pitch angle settings at 75% radius ($\beta_{75,F}$ and $\beta_{75,A}$) are listed in table 1. The rotational speeds of the front and aft rotors are identical at n = 1,100rpm, resulting in a helical tip Mach number of M = 0·73 at the low-speed conditions under study here. In total, the simulations were done at the three angles of attack of $\alpha = -4°$, $\alpha = 0°$ and $\alpha = -4°$ with a DBP sense of rotation. Thanks to the symmetric nature of this generic CROR and pylon geometry along the horizontal plane, the three computed cases yield results that can be interpreted as both an up behind pylon sense of front rotor rotation case at the actual angle-of-attack the simulation was run for and as a down behind pylon case at an angle-of-attack with the opposite sign, for a total of six operating points of the engine. For each angle-of-attack the blade setting angles are set to obtain the nominal take-off thrust setting with a power split of P_F/P_A = 1·25 between the two rotors.

Table 1
Sense-of-rotation dependent engine operating point definitions

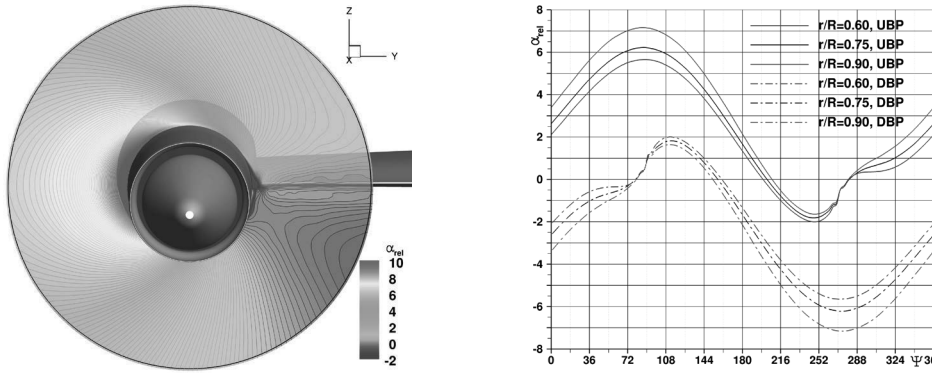
	Front Rotor			Aft Rotor		Overall	
Analysis Case	α(°)	n_F(rpm)	$\beta_{75,F}$(°)	n_A(rpm)	$\beta_{75,A}$(°)	F_x(kN)	P_F/P_A
UBP @ α = –4° & DBP @ α = 4°	–4	1,100	35·60	1,100	40·75	88	1·25
UBP @ α = 0° & DBP @ α = 0°	0		34·85		41·40		
UBP @ α = 4° & DBP @ α = –4°	4		34·05		42·05		

4.1 Aerodynamic analysis

The disparate installation effect impact on the blades for the two opposing senses of front rotor rotation is shown in Fig. 10, where the effective incidence angle variation due to the installation is plotted. The sinusoidal incidence angle variation due to the angle-of-attack is superimposed with the abrupt increase upon passage through the pylon wake. For the DBP sense of front rotor rotation, the AoA-induced increase coincides with that due to the interaction with the pylon. This leads to larger peak blade loadings for this case than for the UBP installation. Figures 11(a) and 12(a) compare the development of a front and aft rotor blades total loading coefficient during one revolution for the two rotational directions.

In the plots, the up-behind-pylon sense of rotation results are shown as light and dark blue lines for the two selected angles of attack of $\alpha = 0°$ and $\alpha = 4°$ respectively, while orange and red lines are used for the alternate down-behind-pylon rotational direction. Clearly evident is the dominant effect of the pylon wake impingement, which causes an abrupt increase in blade loading at an azimuthal position of approximately $\Psi = 265°$, for the UBP and at roughly $\Psi = 85°$ for the DBP sense of rotation. In all cases the non-uniform inflow due to the pylon as well as the mutual interaction between the pylon and the rotors leads to an azimuthal variation in the front blade loading, which is significantly increased by the engine angle-of-attack for the cases at $\alpha = 4°$. The overall amplitude of the 1P-loading fluctuation at angle-of-attack is much greater for the DBP case, where the pylon wake deficit adds to the already increasing loadings during the blades downward sweep. This is also evident in the spectral analysis of the front

https://doi.org/10.1017/S0001924000009829 Published online by Cambridge University Press



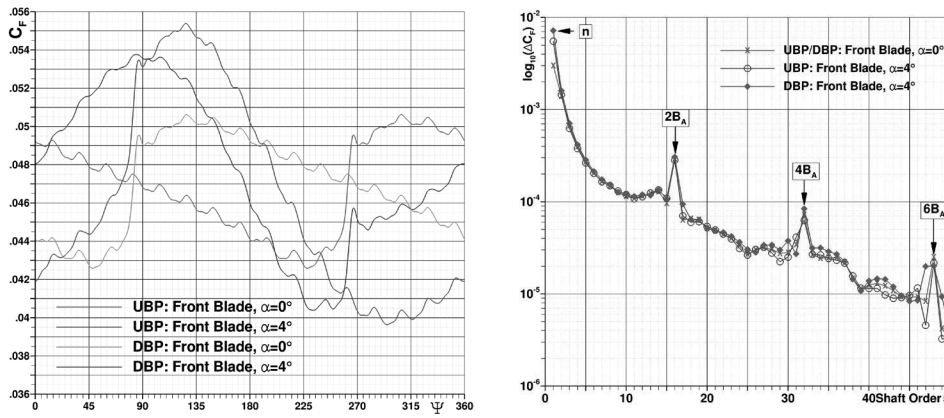
(a) Installation effects on front rotor plane incidence angle distributions

(b) Radial variation of blade sectional effective incidence angle

Figure 10. Combined installation effect impact of angle-of-attack and pylon on front rotor inflow at α = 4°.

blades' unsteady loading as plotted in Fig. 11(b). Both the UBP and the DBP sense of rotation cases at the angle-of-attack of α = 4° show clearly increased loadings at a frequency of $f = n$, i.e. the shaft rotational speed, versus the axial flow case. The largest 1P-loading cycle amplitude is found for the DBP front blade. The blade-blade interaction driven unsteady loadings of the front blade, a 16-cycle fluctuation due to the twice-per-rotation interaction with each of the 8 aft rotor blades, show much smaller variations between all cases, as evidenced by the near coincident peaks at the even number higher harmonics of the aft blades' passing frequency BA in the spectral analysis in Fig. 11(b).

For the aft rotor, the pylon wake impact on the blade loading is also clearly evident. As plotted in Fig. 12(a), while the amplitude of the associated loading increase is not significantly different than that seen for a front blade, its' slope is more gradual. This is indicative of the dissipative effect the interaction with the front rotor has on the coherence of the pylon wake. The dominant aft blade loading at the frequency of $f = n$ is of similar magnitude as was seen for the front blade. However, for the CROR at α = 4° the UBP sense of rotation of the front rotor leads to a higher

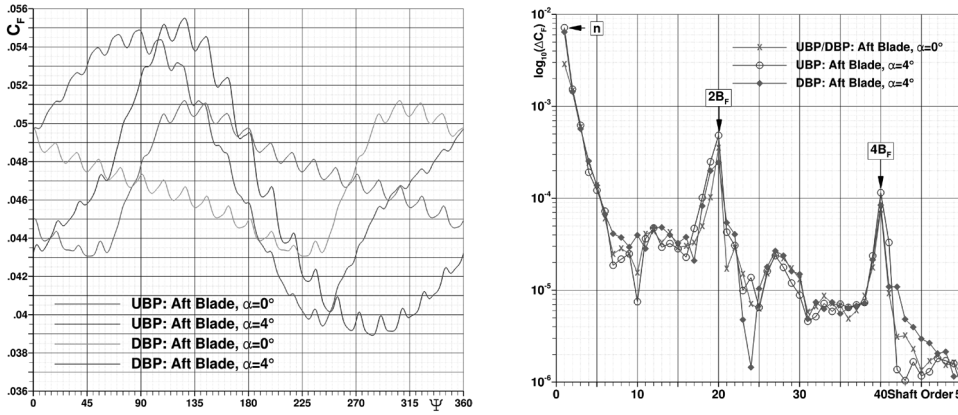


(a) Time history of blade loading development

(b) Spectral analysis of blade unsteady loadings

Figure 11. Installation and sense of rotation impact on CROR front blade total loading.

https://doi.org/10.1017/S0001924000009829 Published online by Cambridge University Press



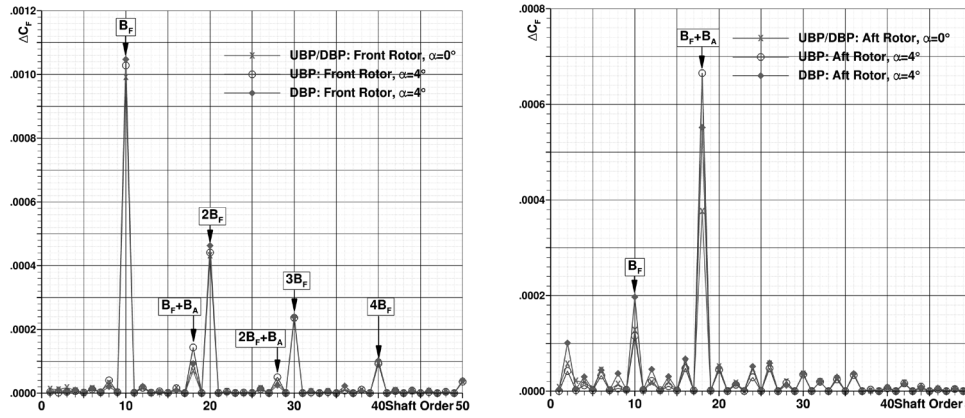
(a) Time history of blade loading development (b) Spectral analysis of blade unsteady loadings

Figure 12. Installation and sense of rotation impact on CROR aft blade loading development.

1P-loading cycle for an aft blade, albeit with a relatively modest increase over the DBP case. The explanation for this is analogous to that presented for the front rotor, with the increased blade loadings during the downward sweep of the aft blade on the UBP case coinciding with the blades interaction with the pylon wake. The periodic impingement of front rotor blade wakes on the aft blade leads to a 20-cycle fluctuation in the aft blade loadings, as the latter passes behind each of the front rotors 10 blades twice during one rotation. This unsteady loading shows up as the peaks at even number higher harmonics of the front rotors blade passing frequency BF in Fig. 12(b). Here the differences between the various cases are more evident, with the fluctuation amplitudes for the UBP case at $\alpha = 4°$ noticeably larger than that of the DBP case at the same angle-of-attack. This is indicative of more pronounced front rotor blade wakes in the former case, which is a consequence of a higher mean front rotor loading. This can be seen in the summary of the mean rotor performance data in Table 2, where the blade setting to achieve the common operating point shifted the thrust production more to the front rotor for the UBP case in comparison to the DBP sense of rotation. In addition, the aft blades are at least partially affected by the impingement of the front blade tip vortices as they pass aft of the more highly loaded front rotor blades on the latters' downward sweep[19]. The azimuthal variation of this blade-vortex interaction, as well as the variable front blade wake strength caused by the dependence of the blade loading on the angle-of-attack and pylon induced inflow perturbations, were found by Brandvik, Hall and Parry[20] to be the root cause of the multiple sidebands found at the modulation frequencies around the primary interaction frequencies of $2B_F$ and $4B_F$ in Fig. 12(b). For the front blade spectra in Fig. 11(B), a similar effect is seen at least for the higher harmonic interaction frequeny of $6B_A$.

The impact of the rotor-rotor-interaction as well as the pylon wake impingement at the rotor level is plotted in the rotor unsteady loading spectra in Fig. 13. The plot shows the dominant front rotor loading variations occurring at the front rotors blade passing frequency as well as the higher harmonics thereof. This is related to the pylon wake impingement on each of the ten blades and only a small increase in the fluctuation amplitudes is found for the cases at the higher angle-of-attack of $\alpha = 4°$. Consistent with the observations previously made at the blade level, the fluctuation amplitude for the DBP sense of rotation is slightly larger than that of the UBP case. Quite notably, the loading cycle of the rear rotor shows a negligible response at the aft rotors blade passing frequency. Instead, the dominant frequency is the first interaction frequency of

https://doi.org/10.1017/S0001924000009829 Published online by Cambridge University Press



(a) Spectral analysis of front rotor unsteady loading (b) Spectral analysis of aft rotor unsteady loading

Figure 13. Angle-of-attack and sense of rotation impact on rotor unsteady loadings.

$f = B_F+B_A$, with another smaller peak visible at the front rotors blade passing frequency. As the pylon wake is dissipated to a great degree in its interaction with the front rotor, the aft blades respond to the strong pylon-induced loading cycle of the front blades. Since the relative position of an aft blade versus a front blade during the latter's interaction with the pylon wake varies due to the differing blade counts in both rotors, the dominant frequency of the aft rotor loading is the first order interaction frequency. As the angle-of-attack grows, a significant increase in the amplitude of this fluctuation versus the case at $\alpha = 0°$ is seen. Consistent with the discussion of the blade unsteady loadings, here the UBP case shows a larger unsteady loading at $f = B_F+B_A$ than occurs for the DBP case.

The rotor performance in terms of front and aft rotor thrust and power are summarised in Table 2, with all data based on the forces acting on the blades only, i.e. omitting the contributions of the hubs and spinner. In all cases, the required take-off thrust for the isolated powerplant of $F_x = 88$kN is achieved at the desired rotor power balance of $P_F/P_A = 1{\cdot}25$ with an overall efficiency level of between $\eta = 57{\cdot}49\%$ and $\eta = 58{\cdot}14\%$.

Table 2
Sense of rotation impact on mean rotor performance

		UBP, $\alpha = 0°$	UBP, $\alpha = 4°$	DBP, $\alpha = 0°$	DBP, $\alpha = 4°$
Front Rotor	C_T	0·3915	0·4009	0·3915	0·3818
	C_P	0·5793	0·5736	0·5793	0·5838
	$C_{F,1P}$	0·008764	0·016083	0·008764	0·021383
	Ψ_{1P} (°)	266·87	343·87	86·87	38·49
Aft Rotor	C_T	0·2883	0·2783	0·2883	0·2968
	C_P	0·4647	0·4605	0·4647	0·4678
	$C_{F,1P}$	0·007396	0·018837	0·007396	0·016476
	Ψ_{1P} (°)	272·40	329·94	92·40	20·61
Overall	F_x (N)	88,241	88,157	88,241	88,086
	P_F/P_A	1·2467	1·2457	1·2467	1·2479
	η (%)	57·83	58·14	57·83	57·49

https://doi.org/10.1017/S0001924000009829 Published online by Cambridge University Press

Additionally, Table 2 lists the mean rotor in-plane force coefficient CF,1P, which is the vector sum of the lateral and lift force coefficients CY and CZ, for the computed CROR operating points at low-speed flight conditions as evaluated for the differing sense of rotation. The data shows that the inflow distortion induced by the pylon is significant and leads to the production of large in-plane forces for both rotors even at the angle-of-attack of $\alpha = 0°$. The total blades-only front rotor 1P-loading of CF,1P = 0·008764 represents 2·24% of the front rotor thrust, while the rear blades value of CF,1P = 0·007396 equates to 2·57% of the aft rotors thrust. For both front rotor senses of rotation, the 1P-loads of both rotors act in the direction of the pylon, with only a very small lift component.

For the CROR at $\alpha = 4°$ the overall magnitude of the front and aft rotor in-plane forces reaches values of around 4·01% and 6·76% of the respective rotors thrust for the UBP case and 5·60% and 5·56% for the DBP sense of rotation. Figure 14 visualises the resulting force vectors as they would appear on a notional T-tail aircraft configuration. The clear asymmetry in the 1P-loads of the left and right, i.e. the UBP and DBP, engine, along with the not insignificant lever arm versus the centre of gravity would lead to the need to trim for this asymmetry at the aircraft level. As can be seen in the vectors as well as from the values in Table 2, the discrepancy in the lateral 1P-forces between the left and right engine in particular are of concern. Additionally, the sensitivity of the rotor in-plane forces to the engine and the aircraft operating point leads to a dynamic variation of these forces during maneuvers for example, placing additional requirements on the aircraft flight control system.

The close coupling of the pylon with the front rotor has a notable impact on the aerodynamics of the pylon. This interaction leads to a mean steady effect on pylon aerodynamic coefficients as well as strong unsteady oscillations thereof. The former is result of the acceleration of the flow into the front rotor. Figure 15(a) compares the pylon lift coefficient time history as a function of rotor azimuth angle for the nacelle angle-of-attack of $\alpha = 4°$, drawing on the results for the UBP and DBP cases. Also included are results of a steady RANS analysis of the engine in blades-off/power-off configuration. The mean effect of the flow acceleration into the rotors for the power-on versus the power-off case is evident when comparing the dash-dotted red and blue lines versus the solid light blue line. For the power-on cases an increase in the magnitude of the lift coefficient is found, with

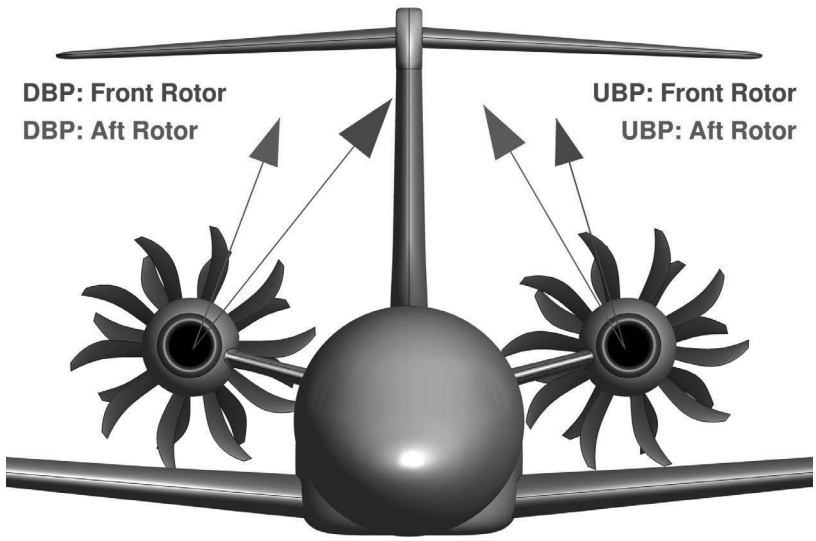
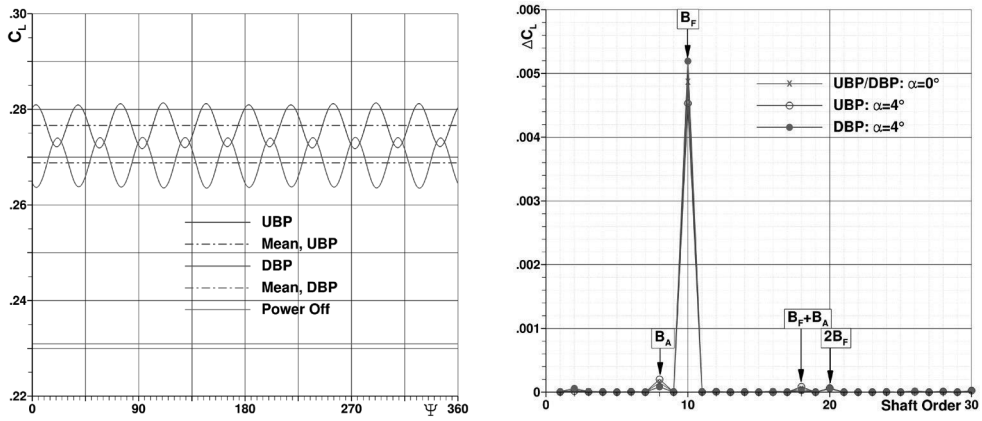


Figure 14. Asymmetric 1P-loads resulting from common sense of rotation installed CRORs.

https://doi.org/10.1017/S0001924000009829 Published online by Cambridge University Press



(a) Pylon lift development at angle-of-attack α = 4° (b) Spectral analysis of pylon lift fluctuation

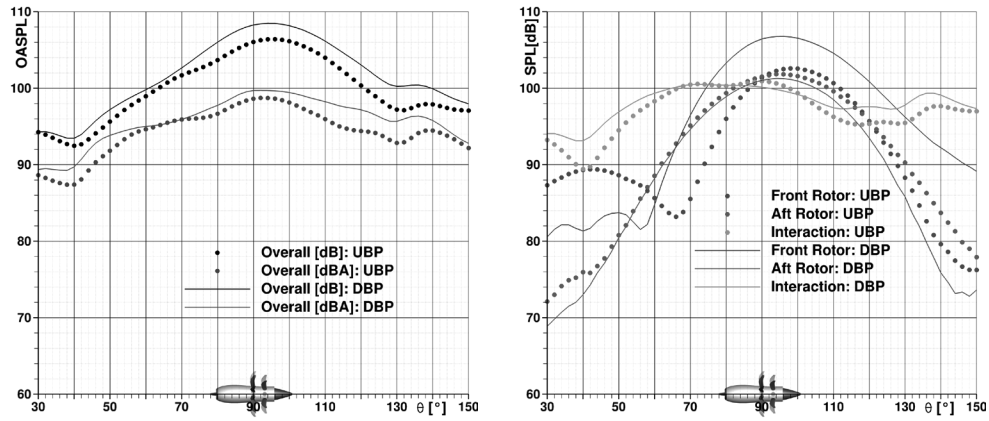
Figure 15. Angle-of-attack and sense of rotation impact on pylon lift development.

the sense of rotation also playing a role. Reduced pylon lift occurs for the DBP sense of front rotor rotation at the angle-of-attack of α = 4°. Significant unsteady loadings due to the rotors are found for the pylon, with a periodic 10-cycle oscillation around the mean value evident. Figure 15(b) plots the spectral analysis of the pylon lift coefficient fluctuations C_L versus the shaft order for the engine at α = 4°. The dominant source of unsteadiness is linked to the passage of the front rotor blades, with the largest amplitude fluctuation occurring at the front rotor's blade passing frequency. A small contribution to the unsteady loading also occurs at the aft rotor's blade passing frequency, as well as at the first order interaction frequency, indicating at least a minor interaction between the aft blades and the pylon flowfield. Again, the sense of rotation is seen to cause a difference in the unsteady pylon lift loading, with the higher front blade loads during passage behind the pylon of the DBP case at α = 4° leading to a larger fluctuation amplitude at the frequency of $f = B_F$ than for the UBP sense of rotation. As expected, the opposite is true for the pylon unsteady loading at $f = B_A$, as an aft rotor blades has a higher loading during its' passage aft of the pylon for the UBP sense of front rotor rotation than for the DBP case.

4.2 Aeroacoustic analysis

The influence of the rotor interaction with the pylon and the alternate senses of rotation on the overall farfield noise emissions for the community noise case is plotted in Fig. 16 for a single CROR at an angle-of-attack of α = 4°. In both subfigures the results of the DBP sense of front rotor rotation are shown as solid lines, while the UBP data is plotted using circular symbols. Figure 16(a) shows the overall noise emission characteristics as well as the impact of A-weighting on the overall sound pressure level polar directivity. Figure 16(b) compares the decomposition of the polar directivities into rotor associated and interaction tones for the two senses of rotation. In the directivities, the DBP case shows a noise penalty for the peak ground noise emissions as well as the overall noise levels throughout the investigated polar arc. The highest noise emissions occur in the vicinity of the rotor planes, where a 2dB higher noise level is found in comparison to the UBP case. Generally this magnitude of noise penalty for the DBP case is found for all of the ground array microphones, with a gradual reduction in the difference towards the extreme up – and downstream polar angles. The largest difference is in fact found in the downstream direction for a polar angle of around θ = 130°. A-weighting leads to an overall attenuation of the

https://doi.org/10.1017/S0001924000009829 Published online by Cambridge University Press



(a) Impact of A-weighting on the polar directivity

(b) Tone contributions to the overall sound pressure levels

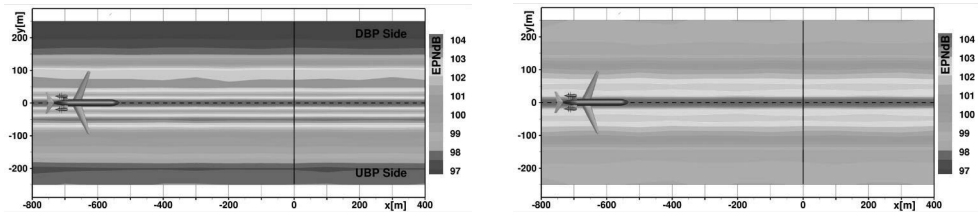
Figure 16. Sense of rotation impact on farfield ground polar directivities for the CROR at α = 4°.

noise levels for both CROR senses of rotation. The greatest reductions of around 9dB versus the unweighted levels are found in the direct vicinity of the rotors, where the lower-frequency rotor tones dominate. In the up – and down-stream arc, where the higher frequency interaction tones become the dominant noise source, smaller differences of around 4dB due to the weighting impact are found. This is a clear indication of the important contribution of the interaction tones to the perceived noise levels of CROR engines.

The blue lines or circles in Fig. 16(b) represent the noise contribution of the front rotor of the DBP and UBP cases respectively. The higher front blade loading for the DBP case in comparison to the UBP case in the lower arc between the azimuth angles of $100° < \theta < 260°$ as was discussed in the aerodynamic analysis (see Fig. 11) translates into a significant noise penalty for the front rotor tones in the former case. Here, the difference in the peak noise levels, found just downstream of the rotors' rotational plane, is almost 5dB. The UBP cases front rotor is only seen to radiate more noise in the upstream arc, possibly driven by the effect of the slightly more pronounced pylon wake in this case. Conversely, and as expected from the analysis of the aft rotor blade loadings in Fig. 12, the aft rotor associated noise radiation, shown in red in Fig. 16(b) is greater for the UBP. At the location of peak noise emission, again just downstream of the rotors' rotational plane, this difference is almost negligible at below 1dB and only grows to notable levels for up – and particularly downstream polar angles. Interaction tone contributions to the ground noise emissions are plotted as green lines or symbols in Fig. 16(b). For these tones, the DBP case is found to have moderately higher noise levels, primarily in the up – and downstream arc. The largest difference is on the order of 2dB in favor of the UBP sense of rotation.

In order to estimate the impact of the rotor sense of rotation on the acoustic ground signature at the aircraft level, a simulation of the flyover noise footprint for two possible engine-airframe configurations is performed. A comparison between an aircraft featuring a common sense of rotation of the CRORs on either side, which equates to an UBP sense of front rotor rotation on one and a DBP sense of rotation on the other, and a configuration with counter-rotating UBP sense of rotation CRORs is done. To approximate these engine-airframe combinations, the UBP and DBP front rotor sense of rotation CROR simulation results at the angle-of-attack of $\alpha = 4°$ are used and combined to obtain the desired configuration for the flyover analysis. The noise footprint in terms of

https://doi.org/10.1017/S0001924000009829 Published online by Cambridge University Press



(a) Common sense of left and right CROR rotation (b) UBP counter rotation of left and right CROR

Figure 17. Comparison of sense of rotation impact on ground noise footprint for aircraft at α = 4°.

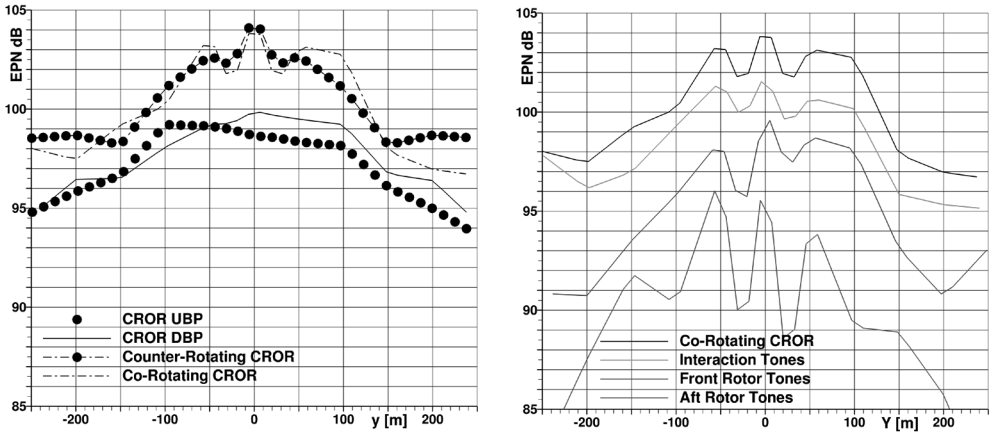
the effective perceived noise level (EPNL) is computed for flight of the notional aircraft at a fixed velocity of M = 0·2 and a fixed altitude of 150m over the centreline of a rectangular ground segment measuring 500m in width and 1,200m in length. The acoustic pressure time history produced by the respective left and right CROR are first summed in the time domain and then transformed into a narrow-band spectrum at each of the 19 × 19 reference points located on a hemispherical surface surrounding the two engines. Based on this data, the flyover noise prediction utilises the HEMISPHERE code[21] to propagate the acoustic to the ground microphones by applying corrections to account for the Doppler effect, spherical spreading, atmospheric absorption and ground reflection and attenuation effects. It is assumed that the noise propagation radially away from the hemisphere can be treated as free propagation and non-linear effects are neglected.

Figure 17 shows the comparison of the effective perceived noise level ground footprint for the co-and counter-rotating CROR configurations. The projection of the flightpath is shown in the plots as a dashed line. In general, the ground noise footprint pattern for both the co-and counter-rotating CROR configurations consists of lines parallel to the flight path, enclosing areas of a certain EPNdB value. For both cases the highest noise value is found around the centreline with level decreases towards the sideline. The counter-rotating CROR configuration shows a symmetric and monotonic decrease with increasing sideline distance, while the co-rotating CROR case leads to an asymmetric pattern with higher levels for most of the sideline than found for the counter-rotating CROR-powered aircraft.

A quantitative assessment is shown in Fig. 18, which plots the EPNL as a function of the sideline distance for a reference axial position of x = 0m, as marked by the solid black lines in Fig. 17. The dashed line and the dashed line with circles in Fig. 18(a) represent the results for the co – and counter-rotating CROR cases respectively, while the solid line and the circles represent the individual contributions from the CROR with the DBP and the UBP sense of front rotor rotations respectively. In general, the position of the maximum EPNL occurs directly around the centreline, with the counter-rotating CROR configuration showing a marginally higher peak noise level in comparison with the configuration with a common sense of rotation for both CRORs. The levels fall off quickly with increasing sideline distance, with a clear advantage seen for the counter-rotating CROR case. Figure 18(a) shows peaks and valleys for both engine-airframe configurations with increasing sideline distance, which are caused by acoustic interference of the two CRORs signal. The higher ground noise for the DBP sense of rotation CROR in comparison with UBP sense of rotation reflects the higher aerodynamic loads on the front blades in the lower arc.

For the co-rotating CROR configuration, Fig, 18(b) shows a breakdown of the EPNL noise signature into tones associated with the front and aft rotor as well as the interaction tone contributions at the reference axial location. The aft rotor associated tones are seen to play the least important role in the overall EPNL for this configuration. The root causes for this can be traced to

https://doi.org/10.1017/S0001924000009829 Published online by Cambridge University Press



(a) Sense of rotational direction impact on perceived noise levels

(b) Tone contributions for common sense of rotation CRORs

Figure 18. Noise footprint as a function of sideline distance at the reference axial location of x = 0m.

the generally lower peak levels of the aft rotor tones versus the front rotor tones, but also to their lower frequency due to the lower blade number. Thus these frequencies are attenuated via the annoyance correction in the EPNL evaluation. One other major reason for the lower contribution of the aft rotor tones to the flyover noise is likely found in the reduced amount of time that high levels of these tones are radiated towards the ground, as their directivities are not as strongly affected by the pylon wake impingement as are the front rotor tones. This inherent correction for the duration of a noise source in the effective perceived noise level assessment is also the main reason that interaction tones are found to be the dominant noise source in Fig. 18(b). The flat interaction tone directivity exhibited in Fig. 16(b) thus more than compensates for their slightly reduced peak levels in comparison with the rotor tones in this noise emission metric. Furthermore, the interaction tones occur at higher frequencies than do the rotor tones. Therefore they are less attenuated by the impact of the EPNL annoyance correction, which has a comparable impact on frequency-specific tone level scaling as does the A-weighting that was discussed for Fig. 16(a).

5.0 CONCLUSION

In a number of numerical studies DLR has investigated a broad range of aspects relating to installation effects of pusher-configuration CROR propulsion systems. It was shown that the adverse impact of the pylon wake impingement on the rotors on blade loadings and noise emissions can be ameliorated at reasonable effort in term of air requirements through the application of pylon trailing-edge blowing. Despite a residual effect of the pylon wake on the front rotor, pylon blowing was found to offer some clear benefits in reducing unsteady blade loadings and the corresponding noise increases in the upstream direction. The decreases in front blade and rotor loading fluctuation amplitudes translate directly into reduced vibration levels and lead to a benefit in terms of blade structural fatigue. While the benefit of pylon blowing in terms of the overall ground noise emission directivities was found to be relatively small in comparison to the installed CROR without pylon blowing, clear reductions in the front rotor tones were achieved, in particular in their upstream radiation. Due to the importance of both the frequency and the length of the exposure to specific

https://doi.org/10.1017/S0001924000009829 Published online by Cambridge University Press

tones in the human ears perception of noise annoyance, a reduction of the relatively high frequency front rotor tones in levels and effective radiation angle for the case with pylon blowing is expected to yield an overall improvement of the perceived noise.

In another study on an important installation effect for pusher CROR configurations it was shown that in combination with angle-of-attack effects, the rotors' interaction with the pylon shows a significant dependence on the selected sense of rotation of the front rotor with respect to the pylon. This aspect can be a concern for the installation of this type of propulsion system on the empennage of an aircraft, where it is expected that counter-rotation of the rotors on the left and right side of the fuselage would most likely be avoided out of cost and complexity concerns. A down behind pylon sense of rotation of the front rotor was confirmed to be less favorable for the blade loadings, as for a typical flight condition with a positive angle-of-attack these are increased on the inboard side by both the pylon wake deficit as well as the angle-of-attack. Thus in-plane loads are increased in comparison to an up-behind-pylon sense of rotation, resulting in the need to trim out asymmetric forces acting on the left and right engine at the aircraft level. In accordance with the impact on the front rotor blade loadings, the down behind pylon sense of rotation also shows increased noise emissions, with a clear penalty for the ground noise emissions and a possible unfavorable impact on the rear cabin noise environment. A flyover noise emission assessment showed that there is a benefit for a symmetric aircraft with counter-rotating CRORs on either side of the fuselage, with a small reduction in noise emissions in the sideline direction along the flightpath versus the case of an aircraft with the same sense of rotation of the rotors on both CRORs.

REFERENCES

1. HAGER, R.D. and VRABEL, D. Advanced Turboprop Project, Technical Report NASA SP-495, NASA, 1988.
2. GERHOLD, T. *Overview of the Hybrid Rans Code TAU, Notes on Numerical Fluid Mechanics and Multidisciplinary Design (NNFM)*, **89**, Springer Verlag, 2005, pp 81-92.
3. YIN, J. and DELFS, J. Improvement of DLR Rotor Aeroacoustic Code (APSIM) and its Validation with Analytic Solution, 29th European Rotorcraft Forum, Friedrichshafen, Germany, 2003.
4. STUERMER, A. Unsteady CFD Simulations of Contra – Rotating Propeller Propulsion Systems, 44th AIAA/ASME/SAE/ASEE Joint Propulsion Conference, AIAA 2008-5218, Hartford, CT, USA, 2008.
5. STUERMER, A. and YIN, J. Low - Speed Aerodynamics and Aeroacoustics of CROR Propulsion Systems, 15th AIAA/CEAS Aeroacoustics Conference, AIAA 2009-3134, Miami, FL, USA, 2009.
6. BLOCK, P.J.W. and GENTRY, G.L. Directivity and Trends of Noise Generated by a Propeller in a Wake, Technical Report NASA TP-2609, NASA Langley Research Center, 1986.
7. PAGE. M.A,, IVEY, D.M. and WELGE, R. Ultra High Bypass Engine Applications to Commercial and Military Aircraft, SAE Paper No. 861720, 1986.
8. FITE, E., WOODWARD, R. and PODBOY, G. Effect of Trailing Edge Flow Injection on Fan Noise and Aerodynamic Performance; AIAA-2006-2844, 3rd AIAA Flow Control Conference; San Francisco, CA, USA, 2006.
9. RICOUARD, J., JULLIARD, E., OMAIS, M., REGNIER, V., PARRY, A.B. and BARALON, S. Installation Effects on Contra-Rotating Open Rotor Noise, AIAA-2010-3795, 16th AIAA/CEAS Aeroacoustics Conference, Stockholm, Sweden, 2010.
10. SEITZ, A., KRUSE, M., WUNDERLICH, T., BOLD, J. and HEINRICH, L. The DLR Project LamAiR: Design of a NLF Forward Swept Wing for Short and Medium Range Transport Application, 29th AIAA Applied Aerodynamics Conference, AIAA 2011-3526, Hawaii, USA, 2011.
11. STUERMER, A., ARNE and YIN, J. Jianping: The Case for Counter-Rotation of Installed Contra-Rotating Open Rotor Propulsion Systems, AIAA2012-2785, 30th AIAA Applied Aerodynamics Conference, 25-28 June 2012, New Orleans, LA, USA.
12. SPALART, P. and ALLMARAS, S. A One-Equation Turbulence Model for Aerodynamic Flows, AIAA1992-0439, 1992.
13. JAMESON, A. Time Dependent Calculations Using Multigrid, with Applications to Unsteady Flows Past Airfoils and Wings; 10th AIAA Computational Fluid Dynamics Conference; Honolulu, HI, USA, 1991.

https://doi.org/10.1017/S0001924000009829 Published online by Cambridge University Press

14. MADRANE, A., RAICHLE, A. and STUERMER, A: Parallel Implementation of a Dynamic Unstructured Chimera Method in the DLR Finite Volume TAU-Code; 12th Annual Conference of the CFD Society of Canada; Ottawa, Ontario, Canada; 524-534; 2004.
15. YIN, J. and AHMED, S. Prediction and its Validation of the Acoustics of Multiblade Rotors in Forward Flight Utilizing Pressure Data from a 3D FreeWake Unsteady Panel Method, 20th European Rotorcraft Forum, Amsterdam, The Netherlands, 1994.
16. KUNTZ, M., HEINRICH, R., PAHLKE, K. and RADDATZ, J. Unsteady Rotor Aerodynamics and Acoustics, 23rd European Rotorcraft Forum, 16-18.9.1997, Dresden, Germany, 1997.
17. FFOWCS WILLIAMS, J. and HAWKINGS, D. Sound generation by turbulence and surfaces in arbitrary motion, **A264**, 1969, pp 321-342.
18. BRENTNER, K. and FARASSAT, F. An analytical comparison of the acoustic analogy and kirchhoff formulation for moving surfaces, *AIAA J*, **36**, (8), 1998, pp 1379-1386.
19. STUERMER, A. and YIN, J. Installation impact on pusher CROR engine low speed performance and noise emission characteristics, *Int J Engineering Systems Modeling and Simulation*, 2012, **4**, (1-2), pp 59-68.
20. BRANDVIK, C.A., HALL, A.B. and PARRY, A.B. Angle-of-Attack Effects on Counter-Rotating Propellers at Take-Off, GT2012-69901, ASME Turbo Expo 2012, Copenhagen, Denmark, June 2012.
21. YIN, J. and BUCHHOLZ, H. Toward noise abatement flight procedure design: DLR rotorcraft noise ground footprints model, *J American Helicopter Society*, 2007, **52**, pp 90-98.

https://doi.org/10.1017/S0001924000009829 Published online by Cambridge University Press